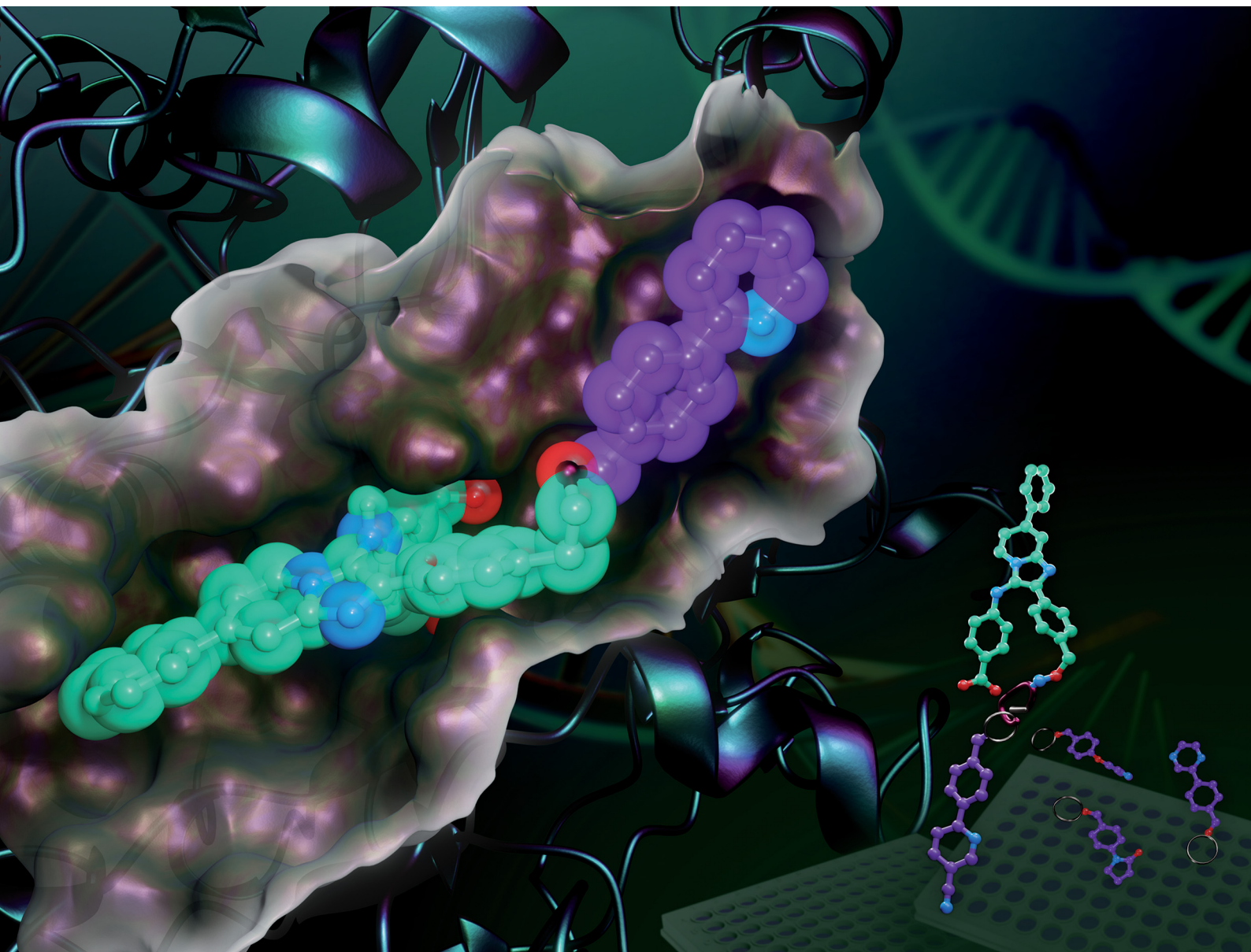


RSC Chemical Biology

rsc.li/rsc-chembio



ISSN 2633-0679

PAPER

Xue Zhi Zhao *et al.*

Identification of multidentate tyrosyl-DNA phosphodiesterase 1 (TDP1) inhibitors that simultaneously access the DNA, protein and catalytic-binding sites by oxime diversification



Cite this: *RSC Chem. Biol.*, 2023, 4, 334

Identification of multidentate tyrosyl-DNA phosphodiesterase 1 (TDP1) inhibitors that simultaneously access the DNA, protein and catalytic-binding sites by oxime diversification†

Xue Zhi Zhao,^a Wenjie Wang,^b George T. Lountos,^c Evgeny Kiselev,^b Joseph E. Tropea,^d Danielle Needle,^d Yves Pommier^b and Terrence R. Burke, Jr.^a

Tyrosyl-DNA phosphodiesterase 1 (TDP1) is a member of the phospholipase D family that can downregulate the anticancer effects of the type I topoisomerase (TOP1) inhibitors by hydrolyzing the 3'-phosphodiester bond between DNA and the TOP1 residue Y723 in the critical stalled intermediate that is the foundation of TOP1 inhibitor mechanism of action. Thus, TDP1 antagonists are attractive as potential enhancers of TOP1 inhibitors. However, the open and extended nature of the TOP1–DNA substrate-binding region has made the development of TDP1 inhibitors extremely challenging. In this study, starting from our recently identified small molecule microarray (SMM)-derived TDP1-inhibitory imidazopyridine motif, we employed a click-based oxime protocol to extend the parent platform into the DNA and TOP1 peptide substrate-binding channels. We applied one-pot Groebke–Blackburn–Bienayme multicomponent reactions (GBBRs) to prepare the needed aminoxy-containing substrates. By reacting these precursors with approximately 250 aldehydes in microtiter format, we screened a library of nearly 500 oximes for their TDP1 inhibitory potencies using an *in vitro* fluorescence-based catalytic assay. Select hits were structurally explored as their triazole- and ether-based isosteres. We obtained crystal structures of two of the resulting inhibitors bound to the TDP1 catalytic domain. The structures reveal that the inhibitors form hydrogen bonds with the catalytic His-Lys-Asn triads ("HKN" motifs: H263, K265, N283 and H493, K495, N516), while simultaneously extending into both the substrate DNA and TOP1 peptide-binding grooves. This work provides a structural model for developing multivalent TDP1 inhibitors capable of binding in a tridentate fashion with a central component situated within the catalytic pocket and extensions that project into both the DNA and TOP1 peptide substrate-binding regions.

Received 18th November 2022,
Accepted 26th March 2023

DOI: 10.1039/d2cb00230b

rsc.li/rsc-chembio

Introduction

Topoisomerases (TOPs) correct DNA topological stress by creating DNA–protein crosslinks (DPCs) during the cleavage of one DNA strand (TOP1 and TOP3) or both strands (TOP2). TOP1 is essential for genomic stability by resolving DNA supercoiling

or knotting that could otherwise result in alternate DNA structures.¹ TOP1 achieves its effects through nucleophilic attack of its Y723 hydroxyl onto a DNA 3'-phosphodiester bond, resulting in the formation of a covalent TOP1–DNA bond with concomitant strand breakage. This generates topoisomerase cleavage complexes (TOPCCs), which are quite transient and rapidly relegated with release of the TOP1 following decatenation of the DNA. In quiescent cells the TOP1CCs are not inherently harmful, however, in highly dividing cells they can be converted into cytotoxic irreversible TOP1CCs and ultimately lead to DNA damaging double-strand breaks.² TOP1 inhibitors, such as the alkaloid camptothecin (CPT), bind at the TOP1–DNA interface, stall relegation of TOPCCs and induce cell death in mitotic cells.^{3,4} The water-soluble camptothecin derivatives topotecan and irinotecan are potent TOP1 inhibitors used for the treatment of ovarian and lung cancers and colorectal cancers, respectively.⁵ However, dose-limiting myelosuppression in combination with additional side effects can reduce

^a Chemical Biology Laboratory, Center for Cancer Research, National Cancer Institute, National Institutes of Health, Frederick, MD, USA.

E-mail: xuezhi.zhao@nih.gov

^b Developmental Therapeutics Branch & Laboratory of Molecular Pharmacology, Center for Cancer Research, National Cancer Institute, National Institutes of Health, Bethesda, MD, USA

^c Basic Science Program, Frederick National Laboratory for Cancer Research, Frederick, MD, USA

^d Center for Structural Biology, Center for Cancer Research, National Cancer Institute, Frederick, MD, USA

† Electronic supplementary information (ESI) available. See DOI: <https://doi.org/10.1039/d2cb00230b>

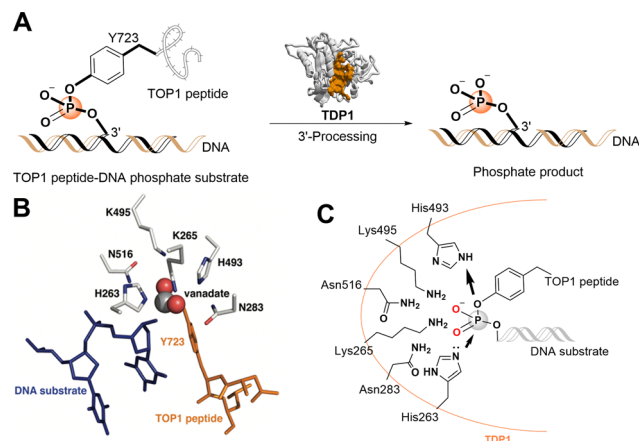


Fig. 1 TDP1 3'-processing reaction and substrates. (A) TDP1 hydrolyses the phosphotyrosyl ester bond between the Y723 residue of the TOP1-derived peptide and the 3'-end of the DNA substrate to generate a 3'-processed phosphate containing product. (B) Structure of a TDP1-vanadate-TOP1 peptide complex. TDP1 (carbon atoms are shown in gray, nitrogen atoms are shown in blue, and oxygen atoms are shown in red) is complexed with a single DNA strand (blue sticks) and TOP1-derived peptide (orange sticks) with the phosphate mimetic vanadate highlighted in a sphere representation (PDB code: 1NOP). (C) Hydrolytic mechanism of the TOP1CC phosphodiester hydrolysis by TDP1 HKN motifs.

the clinical effectiveness of TOP1 inhibitors.⁶ Cytotoxicity of TOP1 inhibitors can also be reduced by cancer cell resistance mediated by DNA repair pathways.⁷

The human tyrosyl-DNA phosphodiesterase 1 (TDP1) is a DNA repair enzyme that promiscuously processes 3'-DNA end blocking lesions using a wide range of synthetic DNA adducts as substrates.⁸ The enzyme is found at low levels in most tissues, but its expression is elevated in nearly all tumors.⁹ TDP1 can rescue the genome from damage arising from persistent TOP1CCs by hydrolysing the Y723-DNA phosphodiester linkage and liberating DNA with a free 3'-phosphate group. Down-regulating TDP1 can enhance the toxicity of phosphodiester-linked DNA adducts, such as TOP1CCs (Fig. 1(A)).^{10–13} TDP1 antagonists may be viewed as TOP1 inhibitor chemosensitizers with a potential to lessen dosage-related toxicity and side effects. Accordingly, TDP1 is recognized as a target for new anticancer therapeutics that could be used in combination with TOP1 inhibitors.^{14–17} Significant effort devoted to developing TDP1 inhibitors has resulted in the discovery of a spectrum of structurally diverse inhibitors (recent examples^{18–21}). However, the understanding of the molecular protein-ligand interactions of most of these inhibitors with TDP1 is unclear and clinical agents have yet to result.^{12,22–24} This raises concerns related to potentially promiscuous mechanisms of action that could impact the rational design of new analogs.^{25,26}

The catalytic mechanisms of TDP1 have been studied using vanadate and tungstate as phosphate mimetics. These can replicate aspects of phosphorylase and phosphatase catalytic transition states in crystal structures and thereby clarify mechanisms of these enzymes.^{27–32} Preliminary insights into how catalytic residues engage the DNA 3'-phosphonamide linkage have been provided by X-ray crystal structures of TDP1 without³³ and with

vanadate or tungstate transition state mimetics bound within the catalytic site and with single-strand DNA and TOP1-derived substrates (Fig. 1(B))^{34–36} as well as crystal structures of TDP1 in complex with double-stranded DNA.³⁷ As a member of the phospholipase D superfamily of enzymes, the TDP1 catalytic pocket contains paired histidine and lysine residues within two conserved histidine-lysine-asparagine catalytic motifs [HxKx(n)N, with x being any amino acid].^{38,39} These residues are arranged to hydrolyse the TOP1CC phosphodiester linkage in a two-step process (Fig. 1(C)).⁴⁰ In the first step, a H263 imidazole nitrogen executes a nucleophilic attack on the 3'-phosphotyrosyl linkage. This releases the tyrosyl residue and associated protein while forming a covalent 3'-phosphonamide linkage with the DNA. The second signature histidine (H493) then donates a proton to the leaving nucleophilic phenoxy anion of the liberated tyrosyl residue.⁴¹ This converts H493 into a basic nucleophile that activates a water molecule to attack the DNA 3'-phosphonamide linkage to H263, thereby releasing the DNA from TDP1. The K265 and N283 residues of the first HKN motif form hydrogen bonds with the 3'-phosphoryl group, while the K495 and N516 residues of the second HKN motif stabilize the substrate and function as a relay to protonate/deprotonate the H493 residue.

Progress in the development of TDP1 inhibitors could be facilitated by maximizing interactions of ligands with specific features of the protein catalytic apparatus. TDP1's topographical features are organized to accommodate substrate and execute phosphodiester hydrolysis. Protein-DNA adducts, such as TOP1CCs, present three distinct components: the protein adducted to DNA, the DNA polynucleotide chain and the 3'-phosphodiester crosslink between the two. Accordingly, interaction of the trimeric TOP1CC with TDP1 occurs within three functional regions. The tyrosyl-3'-phosphodeoxyribose ester binds in a well-formed pocket containing the catalytic pocket, while a narrow (approximately 8 Å wide) positively charged channel extends from one side of the catalytic pocket to accommodate the negatively charged DNA polynucleotide chain. A wider, more neutral concave region extends in the opposite direct from the catalytic pocket to hold and align the TOP1-derived peptide moiety. The width of this region expands from 8 Å near the active site to as wide as 20 Å.⁴⁰

The design of TDP1-binding small-molecule ligands could benefit by taking advantage of the tripartite nature of the interaction of TDP1 with TOP1CC substrates, exploiting structural components capable of accessing the catalytic pocket as well as the DNA- and peptide-binding channels. The TDP1-binding affinities of the resulting multivalent ligands could potentially be significantly enhanced relative to those of monovalent ligands due to thermodynamic considerations.^{42,43} In spite of the fact that increases in molecular size and complexity required to realize these multidentate interactions may place such compounds outside parameters defined by the "Lipinski rule of 5",⁴⁴ this does not necessarily limit their suitability as drug candidates.⁴⁵

Although the catalytic pocket is organized to recognize phosphate esters, phosphates suffer from several disadvantages that render them unattractive for ligand design. For this reason, bioisosteres are frequently used to replicate biological



interactions of phosphates.⁴⁶ Recently, we employed an X-ray crystallographic screen of TDP-binding small molecule fragments, which lead to the discovery of phthalic acids and quinolone-based motifs that engage the catalytic core of TDP1 in a fashion similar to the previously described vanadate phosphate mimetics.⁴⁷ We then employed Alexa Fluor 647 (AF647)-tagged TDP1(148-608) as a fluorescent probe and evaluated its ability to bind to a small-molecule microarray (SMM) against 21 000 drug-like small molecules.⁴⁸ In this way we identified the imidazopyrazine nucleus as a TDP1-binding motif. Further structural variation of the core heterocycle skeleton using one-pot Groebke-Blackburn-Bienayme multicomponent reactions (GBBRs) identified 2-phenylimidazo[1,2-*a*]pyridines (**1** and **2**) having higher inhibitory potencies (Fig. 2(A)). The crystal structure of **3** bound to TDP1 (PDB code: 6W7K) showed that it replicates important interactions with the catalytic phosphate-binding pocket as previously shown by our structurally more simple phthalic acid-containing inhibitors, such as 4-aminophthalic acid.⁴⁷ However, while the phthalic acid moiety anchors the SMM-derived inhibitor within the phosphate-binding pocket, the additional 2-phenylimidazo[1,2-*a*]pyridine nucleus is situated above the phthalic acid phosphate mimic, with the pyridine ring directed toward the DNA substrate-binding region and the 2-phenyl group directed toward the more open TOP-derived peptide-binding channel (Fig. 2(B)).

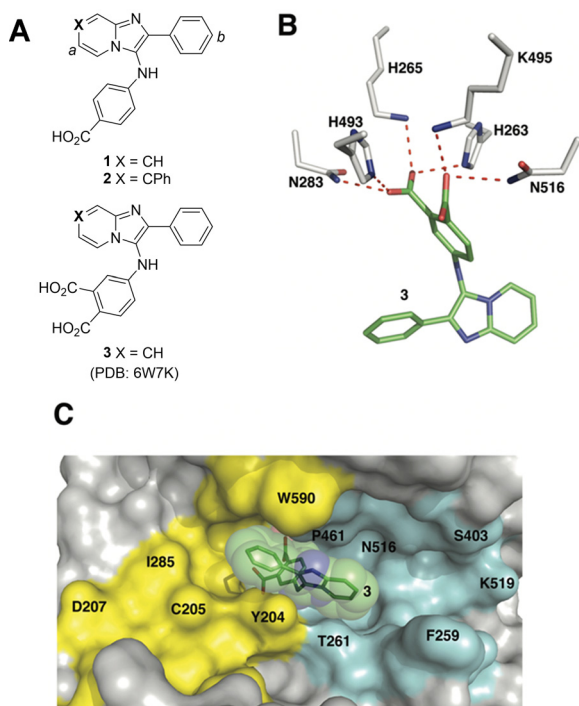


Fig. 2 Structures of TDP1 inhibitors and their binding modes. (A) Structures of the lead TDP1 inhibitors **1–3**. (B) Structure of TDP1 (HKN motif residues are shown as sticks with carbon atoms in gray) complexed to small molecule inhibitor **3** (carbon atoms in green) with hydrogen bonding interactions shown as red dotted lines (PDB code: 6W7K). (C) Small molecule TDP1 inhibitor **3** (carbon atoms are shown in green with transparent green sphere) in the binding regions of the DNA substrate (cyan surface) and a TOP1-derived peptide (in yellow surface) (PDB code: 1NOP).

The 2-phenylimidazo[1,2-*a*]pyridine nucleus represents a platform for construction of trivalent ligands that could potentially simultaneously access the catalytic phosphate-binding pocket and the neighbouring DNA and peptide-binding channels (Fig. 2(C)). This is significant, since multivalency affords a well-known means of achieving significant enhancement in binding affinity.^{42,43} The objective of our current study was to install functionality into the parent platform that would extend into the substrate-binding channels. We were particularly interested in utilizing approaches that would be amenable to parallel structural diversification in microtiter format. “Click chemistry” was coined by Sharpless more than 20 years ago to describe a genre of high-yield reactions capable of facily ligating building blocks using simple reactions, benign solvents and readily available starting materials to produce modular products that require simple isolation techniques.^{49,50} Oxime ligation is a form of click chemistry in which aminoxy-containing molecules react with aldehyde or ketone-containing molecules to join two reactants together through oxime bonds. The oxime bonds are typically biocompatible and stable at neutral pH.^{51–54} We have found that oxime diversification strategies are powerful approaches to rapidly generate libraries of tethered fragments.^{55–58} In contrast to imines, which can undergo rapid hydrolysis in aqueous solutions,⁵⁹ oxime products are chemically stable and can be stored for extended periods without degradation.^{52,54,55} In our current paper, we report application of an oxime-based diversification strategy to prepare a microtiter library of more than 500 analogs having functionality appended onto the 2-phenyl and 7-phenyl rings of the parent imidazo[1,2-*a*]pyridine nucleus (R^a and R^b groups in general structure **4**, Fig. 3(A)). We directly screened the reaction products at two concentrations in *in vitro* gel-based TDP1 inhibition assays. Secondary assays having more data points were run for promising analogs. The added new functionality introduces projections into the DNA and peptide substrate-binding channels.

This work resulted in the identification of oximes that exhibit submicromolar TDP1 inhibitory potencies. X-ray crystal structures of lead compounds bound to TDP1 show that these small molecules can form hydrogen bonds with the catalytic HKN motifs while simultaneously extending into both the DNA substrate- and TOP1 peptide-binding grooves. This validates our original design hypothesis and provides the first trivalent platforms that can access the catalytic site and DNA- and TOP1 peptide substrate-binding regions. The multivalent nature of these interactions provides a model for developing more efficient TDP1-binding ligands.

Results and discussion

Overview of the oxime-diversification strategy

We employed a click-based oxime diversification similar to what we have previously successfully applied to optimize ligands directed at a variety of biological targets (Fig. 3).^{55–58} Keys to this approach are that reactions can be run in DMSO



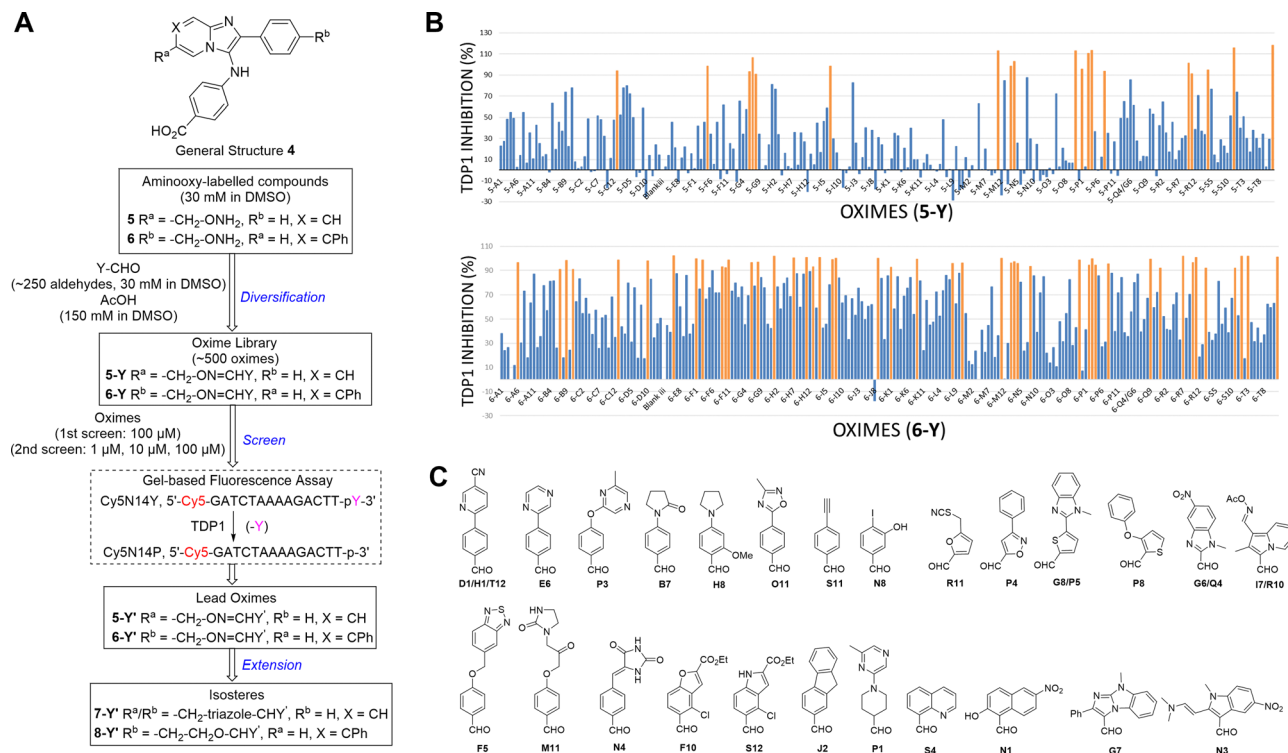


Fig. 3 Schematic overview of oxime-diversification workflow. (A) Three steps of diversification are indicated in blue: (1) diversification of aminooxy-labelled compounds (**5** and **6**) by parallel conversion to oximes (**5-Y** and **6-Y**) by reacting with aldehydes (Y-CHO) in a 96-well plate format; (2) screening of the oxime library (**5-Y** and **6-Y**) using an *in vitro* gel-based TDP1 fluorescence assay to identify lead oximes (**5-Y'** and **6-Y'**); (3) conversion of lead oximes to triazoles (**7-Y'**) and ether-based isosteres (**8-Y'**). (B) Inhibitory screen of oximes at a single concentration of 100 μ M in an *in vitro* gel-based TDP1 fluorescence assay. A total of 19 oximes in the **5-Y** series library and 47 oximes in the **6-Y** series library showed greater than 90% inhibition (in orange). (C) Structures of hit aldehyde precursors from primary screen.

with a slight (5-fold) molar excess of acetic acid and that products are formed in high yield of sufficient purity for direct biological evaluation without purification. This required the availability of the aminooxy-labelled imidazopyridines **5** and **6**, which we prepared using one-pot GBBR synthetic protocols.^{60–63} Synthetic details are presented in the ESI† (Schemes S1 and S2). We anticipated that positioning of aminooxy handles on **5** and **6** would allow the product oxime fragments to project into the substrate-binding channels. The aminophthalic acid moiety appended to the 3-amino substituent on the imidazo[1,2-*a*]pyridine nucleus should nestle securely within the central phosphate-binding catalytic pocket (Fig. 2(C)).

Oxime ligation of the aminooxy substituents was accomplished using the following strategy: (1) The aminooxy-labelled precursors (**5** and **6**, 30 mM in DMSO) were reacted with a library of aldehydes **A1–T12** (Y-CHO, 30 mM in DMSO; approximately 250 aldehydes as shown in Table S1, ESI†) in the presence of acetic acid (150 mM) to yield a final library of oximes (**5-Y** and **6-Y**, 10 mM in DMSO), which were directly evaluated against TDP1 without purification (Fig. 3(A)). (2) All library members were diluted by adding TDP1 reaction buffer (50 mM Tris-HCl, pH 7.5, 80 mM KCl, 2 mM EDTA, 1 mM DTT, 40 μ g mL⁻¹ bovine serum albumin and 0.01% Tween 20) to yield 100 μ M solutions and then screened in an *in vitro* gel-based fluorescence assay to measure inhibitory activity against

TDP1 (1 nM DNA Cy5N14Y, 40 pM TDP1).^{47,48} Compounds that showed promising inhibition (>90% inhibition at 100 μ M) were subjected to re-evaluation at three different concentrations (1 μ M, 10 μ M, 100 μ M) (Fig. 3(B), Tables S2, S3 and Fig. S1, S2, ESI†). A total of 19 oximes in the **5-Y** series library and 47 oximes in the **6-Y** series library showed good (>90%) inhibition. Notably, the oxime products in both 5- and 6-series resulting from reactions with the same aldehydes having 2-phenylpyridine moieties (**D1**, **H1** and **T12**) showed reproducibly good TDP1 inhibition (>90%) in repeat tests (Fig. 3(C)). Oximes **6-B7** and **6-E6** also showed good inhibition (>90%). We conducted a secondary screen of the lead oximes at three different drug concentrations (1 μ M, 10 μ M, and 100 μ M) in gel-based TDP1 inhibition assays (Fig. S2, ESI†). Oximes from aldehydes **B7**, **D1**, **E6**, **M10**, and **P3** showed TDP1 inhibition between 10 μ M and 100 μ M in this secondary screen (Fig. S2, ESI†). (3) A sub-group of oximes (**5-Y'** and **6-Y'**) was then subjected to HPLC purification and structure confirmation by NMR and mass spectrometry. For a select set of promising compounds as based on the structures of aldehyde hits (Fig. 3(C)), we replaced the oxime groups with isosteric triazole or ether moieties (**7-Y'** and **8-Y'**, respectively, Fig. 3(A)).

Biological evaluation of oxime leads

Based on the results of the preliminary screens, we prepared the most promising oximes on a larger scale, and the products



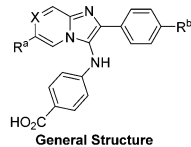
were subjected to HPLC purification (**5-D1**, **5-P3**, **6-D1**, **6-E6**, **6-B7**, **6-P3**, **6-M10**; Table 1 and Fig. S3, ESI†). During the HPLC purification, we identified two products having different retention times but with identical molecular weights as shown by liquid chromatography–mass spectrometry (LC–MS). The major and minor products were consistently present in an approximate 95 : 5 ratio based on absorbance at 254 nm. We assigned the major product as the (*E*)-oxime isomer and the minor product as the (*Z*)-oxime isomer due to anticipated thermodynamic stabilities of the oxime double bond (Table 1). We evaluated the inhibitory potencies of both isomers using TDP1 fluorescence inhibition assays (Table 1).^{64–66} Compounds **5-D1**, **6-D1**, **6-E6**, and **6-B7** showed single-digit micromolar TDP1 inhibitory potencies. For the 5-series oximes, the major (*E*)-**5-D1** isomer ($IC_{50} = 17.4 \pm 3.2 \mu M$) showed greater potency than the minor (*Z*)-**5-D1** isomer ($IC_{50} = 50.3 \pm 10.7 \mu M$). However, this represents an approximate 2-fold loss in potency relative to that of the parent compound **1** ($IC_{50} = 7.87 \pm 2.24 \mu M$). A minor structural change to yield **5-P3** ($IC_{50} > 100 \mu M$) led to a significant decrease in TDP1 inhibitory potency. Among the 6-series oximes, the (*E*)-isomers of **6-D1** and **6-E1** showed approximately 10-fold higher inhibitory potencies than the corresponding (*Z*)-isomers. In the 6-series oximes **6-B7**, **6-P3** and **6-M10**, the (*Z*)-isomers showed slightly better inhibitory potencies than their corresponding (*E*)-isomers. Several oximes, including (*E*)-**6-D1**, (*Z*)-**6-D1**, (*E*)-**6-E6** and (*Z*)-**6-B7**, showed single-digit inhibitory potencies, with (*E*)-**6-E6** exhibiting an IC_{50} value of $3.1 \pm 0.5 \mu M$. The lead oxime (*E*)-**6-D1** displayed a potency ($IC_{50} = 0.38 \pm 0.06 \mu M$) that was 10-fold greater than that of the parent compound **2** ($IC_{50} = 2.98 \pm 0.24 \mu M$). Based on these results, we selected (*E*)-**6-D1** for isostere replacement.

Isosteric replacement of the linker functionality

Having identified preferred aryl fragments (R^a and R^b , Table 1), we replaced oxime-based linker segments with triazole and ether functionalities (Table 2). Heterocycles can serve as useful isosteres and triazoles have particular utility, because of their chemical stability and the fact that they can be readily formed by Huisgen copper catalysed alkyne-azide [3+2] cycloaddition (CuAAC) reactions.^{49,67,68} To replace the (*E*)-oxime linkage in lead (*E*)-**6-D1**, we prepared a series of triazole-linked analogs **7a–e** using CuAAC reactions (Scheme S3, ESI†).⁶⁹ We also prepared the ether-linked analogs **8a, b** and the phthalic acid-containing imidazopyridines **9a–c** with and without the ether-linked biaryl ring (synthetic details in Schemes S3–S5, ESI† and Table 2).

While keeping the phenylpyridine skeleton from the oxime lead (*E*)-**6-D1**, we prepared a series of analogs with triazole (**7a–e**) and ether (**8a, b**) linkers (Table 2, Schemes S3, S4 and Fig. S4, ESI†). Among compounds with triazole linkers on the “left side” (R^a), **7a** showed poor TDP1 inhibition ($IC_{50} = 66.4 \pm 3.7 \mu M$). Placement of the triazole on the “right side” (R^b) gave **7b** ($IC_{50} = 21.6 \pm 5.0 \mu M$), indicating that the compound is 3-fold more potent than **7a**. Increasing the linker length in **7b** reduced inhibitory potency (**7c**, $IC_{50} = 60 \pm 17 \mu M$) compared to that of **7b**, while inclusion of a 4-phenyl group further increased the

Table 1 Structures and inhibitory potencies of oxime lead compounds and derivatives determined by an *in vitro* gel-based fluorescence TDP1 inhibition assay

 General Structure				
 Aminoxy compounds: 5 $R^a = -CH_2ONH_2$, $R^b = H$, $X = CH$; 6 $R^b = -CH_2ONH_2$, $R^a = H$, $X = CPh$ Oximes: 5-X' $R^a = -CH_2ON=CHY'$, $R^b = H$, $X = CH$; 6-X' $R^b = -CH_2ON=CHY'$, $R^a = H$, $X = CPh$				
Compound	X	Structure ($-CH_2ON=CHY'$)	Isomer	TDP1 IC_{50}^b (μM)
5-D1^a	CH	$R^a =$	Mixture ^a	94%
		<i>E</i>		17.4 ± 3.2
		<i>Z</i>		50.3 ± 10.7
5-P3	CH	$R^a =$	Mixture ^a	111%
		<i>E</i>		> 100
		<i>Z</i>		> 100
6-D1	CPh	$R^b =$	Mixture ^a	99%
		<i>E</i>		0.38 ± 0.06
		<i>Z</i>		5.65 ± 3.29
6-E6	CPh	$R^b =$	Mixture ^a	102%
		<i>E</i>		3.1 ± 0.5
		<i>Z</i>		65.3 ± 17.8
6-B7	CPh	$R^b =$	Mixture ^a	91%
		<i>E</i>		10.2 ± 0.33
		<i>Z</i>		7.67 ± 2.3
6-P3	CPh	$R^b =$	Mixture ^a	111%
		<i>E</i>		76.3 ± 41.9
		<i>Z</i>		54.2 ± 18.7
6-M10	CPh	$R^b =$	Mixture ^a	36%
		<i>E</i>		67.7 ± 17.6
		<i>Z</i>		63.1 ± 27.5
6-X	CPh	$R^b =$	Mixture ^a of <i>E/Z</i> = 6/1	73 ± 11
1	CH	$R^a = R^b = H$	—	8.72 ± 1.81
2	CPh	$R^a = R^b = H$	—	2.98 ± 0.24

^a TDP1 inhibition of unpurified reaction mixtures (see Tables S2 and S3, ESI) and HPLC-purified oxime isomers. ^b The half maximal inhibitory concentration (IC_{50}) values were evaluated with an *in vitro* gel-based TDP1 fluorescence assay.

inhibitory potency (**7d**, $IC_{50} = 3.3 \pm 0.2 \mu M$) compared to that of **7b**. Additional extension of the linker length in **7d** by one methylene unit resulted in an 8-fold decrease in potency (**7e**, $IC_{50} = 23.5 \pm 3.2 \mu M$). Replacement of the triazole linker in **7b** with an ether linker of similar extension length (**8a**, $IC_{50} = 25.1 \pm 1.25 \mu M$) had little effect on inhibitory potency (**7b**, $IC_{50} = 21.6 \pm 5.0 \mu M$). Replacement of the triazole linker in **7d** with an ether linker of similar extension length (**8b**, $IC_{50} = 2.75 \pm 0.25 \mu M$) also had little effect on inhibitory potency (**7d**, $IC_{50} = 3.3 \pm 0.2 \mu M$).



Table 2 Structures and TDP1 inhibitory potencies of isostere derivatives determined in an *in vitro* gel-based fluorescence assay

General Structure			
Compound	X	Y	TDP1 IC ₅₀ ^a (μM)
7a	CH	H	66.4 ± 3.7
7b	CH	H	21.6 ± 5.0
7c	CH	H	60 ± 17
7d	CPh	H	3.1 ± 0.2
7e	CPh	H	23.5 ± 3.2
8a	CH	H	25.1 ± 1.25
8b	CPh	H	2.75 ± 0.25
9a	CPh	CO ₂ H	> 100
9b	CPh	CO ₂ H	11.3 ± 1.93
9c	CPh	CO ₂ H	19.8 ± 1.35

^a Half maximal inhibitory concentration (IC₅₀) values were evaluated with an *in vitro* gel-based TDP1 fluorescence assay.

Overall, we found that compounds with analogous linker lengths exhibited comparable inhibitory potencies, whereas increasing the linker extension length tended to reduce inhibitory potency. Meanwhile, the inclusion of a phenyl group at the R^a position enhanced inhibitory potency. Lead compounds, including oxime (*E*)-**6-D1**, triazole **7d** and ether **8b**, were selected to evaluate their TDP1 selectivity over TDP2 using *in vitro* gel-based assays (Table S5 and Fig. S5, ESI[†]). Oxime (*E*)-**6-D1** shows 74-fold greater inhibitory potency against TDP1 than against TDP2. Ether **8b** is also 36-fold more potent against TDP1 than against TDP2. Potencies of triazole **7d** are similar, however an 8-fold enhancement was observed against TDP1 relative to TDP2. In the

HCT116 human colon cancer cell line, oxime (*E*)-**6-D1**, triazole **7d** and ether **8b** showed cytotoxicity CC₅₀ values of 4.8 μM, 136 μM, and 4.3 μM, respectively (Fig. S6, ESI[†]). The CC₅₀ values are higher than the TDP1 *in vitro* IC₅₀ values. At concentrations below their CC₅₀ values, compounds (*E*)-**6-D1**, **7d** and **8b** were shown to act synergistically with the TOP1 inhibitor CPT using HCT116 cells (Fig. S6 and S7, ESI[†]). These data are consistent with the compounds selectively targeting TDP1.

X-ray crystallography

As reported above, through an oxime diversification strategy, we arrived at molecules with TDP1 inhibitory potencies in the low micromolar to nanomolar range (**6-D1**, IC₅₀: 0.38 μM; **7d**, IC₅₀: 3.3 μM; **8b**, IC₅₀: 2.75 μM). Obtaining crystal structures of small molecule ligands bound to TDP1 has been proven to be extremely challenging. We have previously observed that the crystallization of complexes consisting of ligands bound within the TDP1 catalytic pocket is favored by an aryl 3,4-dicarboxyl substituent pattern.^{47,48} Therefore, to enhance crystallization, we added a second carboxyl group to the phenyl-imidazo[1,2-*a*]pyridine platform to yield the parent phthalic acid-containing compound **9a**. The corresponding ether linker-modified analogs **9b** and **9c** were also prepared (Table 2 and Scheme S5, ESI[†]). We found that while analogs **9b** and **9c** exhibited micromolar TDP1 inhibitory potencies (IC₅₀ = 11.3 ± 1.93 μM and 19.8 ± 1.35 μM, respectively) the parent compound **9a** lacking the linked biaryl fragment was significantly less potent (IC₅₀ > 100 μM, Table 2).

We obtained high-resolution crystal structures of the TDP1 catalytic domain in complex with compounds **9a** and **9c** at 1.65 Å and 1.81 Å resolution, respectively (Fig. 4 and Table S4, ESI[†]). As observed in our previous crystal structures of TDP1 bound to imidazopyridine-based inhibitors containing dicarboxylate functionalities,^{47,48} we found that compound **9a** binds to the active site pocket with the carboxylate groups engaged in direct hydrogen bonds with the catalytic residues H263, K265, N283, H493, K495, and N516 (Fig. 4(A)). An additional hydrogen bond interaction is observed with the side chain oxygen atom of S399. A bound water molecule, Wa1019, mediates a water-bridged hydrogen bond between the oxygen atom of one carboxylate group on compound **9a** and the amine nitrogen of the K265 side chain. The phenylimidazopyridine platform of **9a** is positioned such that the phenyl rings at the 3- and 7-positions protrude into the peptide- and DNA-binding pockets, respectively. Y204 interacts with the inhibitor *via* a hydrogen bond between the side-chain hydroxyl oxygen atom and the amine nitrogen linker of compound **9a**, and the side chain is positioned such that it also forms an edge-to-face ("T-shape")^{70–72} π–π interaction (4.3 Å) with the phenyl ring at the 3-position of the imidazopyridine, which is positioned within the peptide-binding pocket of TDP1. Typically, the preferred π–π interaction between Trp and the phenyl ring of Phe occurs through the T-shape, with the phenyl ring being edge-to-face with the indole ring.^{73,74} An additional T-shape π–π interaction (4.8 Å) is observed between the side chain phenyl ring of W590 and the 3-position phenyl ring of the imidazopyridine. The phenyl ring at the 7-position of the imidazopyridine



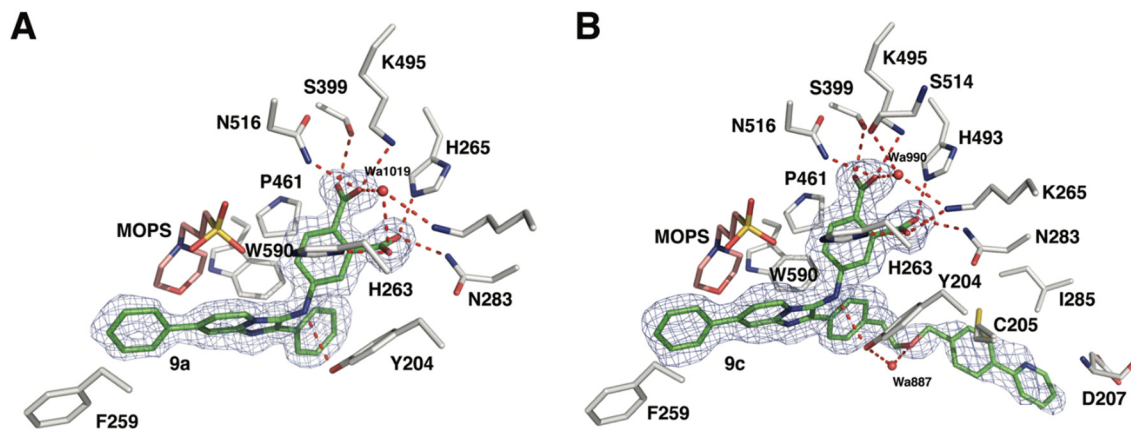


Fig. 4 Crystal structures of TDP1 bound to compounds **9a** and **9c**. (A) The active site of TDP1 (gray sticks) from the crystal structure of TDP1 bound to compound **9a** (PDB code: 8CVQ). The fit of compound **9a** (green sticks) to the final $2F_o - F_c$ electron density map (blue mesh, 1.65 Å resolution, contoured at 1.0 rmsd) is shown. (B) The active site of TDP1 (gray sticks) from the crystal structure of TDP1 bound to compound **9c** (PDB code: 8CW2). The fit of compound **9c** (green sticks) to the final $2F_o - F_c$ electron density map (blue mesh, 1.81 Å resolution, contoured at 0.7 rmsd) is shown.

of compound **9c** extends into the DNA-binding pocket of TDP1 and interacts with the side chain phenyl ring of F259 *via* a parallel-displaced π - π interaction (5.3 Å).⁷⁵ Serendipitously, a MOPS buffer molecule from the crystallization solution is also bound in the active site and is nestled between the imidazopyridine moiety and residues P461 and W590.

Clear electron density was observed in the active site of chain A in the crystal structure of TDP1 soaked with compound **9c** that allowed the placement of the entire molecule of **9c**. However, only partial electron density for compound **9c** was observed in chain B. Chain A-bound **9c** interacts in the same manner as compound **9a** with the catalytic residues. In addition, Wa990 mediates water-bridged hydrogen bonds between the oxygen of one of the carboxylates of compound **9c** with the backbone carbonyl oxygen atom of S399 and the amide nitrogen of the K265 side chain. The π - π interactions between residues Y204, P461 and W590 and the imidazopyridine are also maintained and the side chain of Y204 forms a hydrogen bond to the ether oxygen of **9c**. The appended ether-linked phenylpyridine

moiety extends into the peptide-binding pocket and interacts with the residues lining this pocket, primarily *via* hydrophobic interactions with the side chains of the nonpolar residues C205 and I285 and the aliphatic portion of the D207 side chain. The side chain thiol of C205 also interacts with the phenyl of the phenylpyridine *via* a thiol- π interaction (3.2 Å).⁷⁶ The backbone amide of D207 forms an amide- π interaction⁷⁷ with the pyridine of the phenylpyridine. The carboxylic acid side chain of D207 is also within close distance (3.3 Å) to the 5-carbon of the terminal pyridine, which provides a potential hydrogen bond, possibly between the nitrile in (*E*)-**6-D1** and D207.

Structural basis of inhibition

To gain insights into the structural basis by which compounds **9a** and **9c** exert their inhibitory effect, the coordinates for each complex were superimposed onto the coordinates of TDP1 bound to a TOP1-derived peptide, vanadate, and a DNA substrate; this structure mimics the transition state in the first step of the TDP1 catalytic reaction (Fig. 5). The active site structures

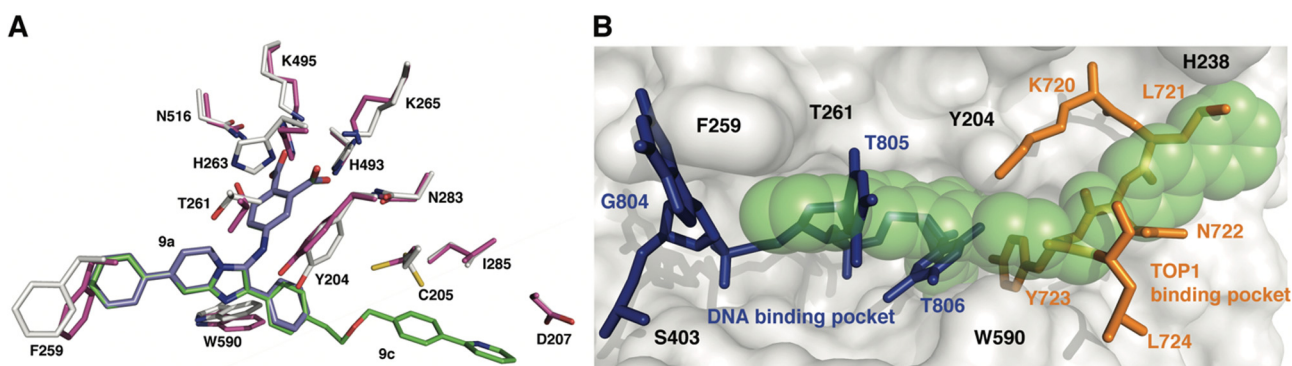


Fig. 5 Structure comparison of TDP1-**9c** complex with the TDP1-vanadate complex. (A) Overlay of the structure of the TDP1-**9c** complex (PDB code: 8CW2), carbon atoms in gray, compound **9c** (carbon atoms in green) onto the coordinates of TDP1 (carbon atoms in magenta) bound to a TOP1-derived peptide and DNA (PDB code: 1NOP). The position of compound **9a** from the TDP1-**9a** complex (PDB code: 8CVQ) is shown in cyan sticks. (B) Surface representation of the active site of TDP1 bound to compound **9c** (represented in green spheres). The position of the DNA substrate (blue sticks) and the TOP1-derived peptide (orange sticks) is shown based on superimposition onto the 1NOP coordinates.



of TDP1 bound to **9a** and **9c** are highly similar. For simplicity, only the residues from the TDP1–**9c** complex are shown superimposed onto the 1NOP coordinates (Fig. 5). The core phenyl-dicarboxylate and phenyl-imidazopyridine scaffold of compounds **9a** and **9c** are essentially in the same position in the overlay. Rotamer shifts are observed for the catalytic residues H263, K265, and K495 when compound **9c** is bound, which results in proper positioning for hydrogen bonding interactions to the dicarboxylate head group. The 7-phenyl ring of the imidazopyridine platform extends into the DNA binding pocket and as a result there is a rotamer shift of residues F259 in order to accommodate the binding of the phenyl ring. In the 1NOP coordinates, F259 is involved in a base stacking interaction with the guanine 804. The appended phenyl ring at the 3-position induces rotamer shifts of the side chains of the neighboring residues Y204 and W590 to optimize their side chain positions for proper hydrogen bonding and π – π interactions with **9c**. Extension of the ether-linked phenylpyridine moiety into the peptide-binding pocket allows for several stabilizing hydrophobic interactions.

We previously demonstrated that the phenyl-dicarboxylate headgroup of the bound compound **9c** (green spheres) mimics the position of the phosphoryltyrosine substrate (Fig. 5(B)). The imidazopyridine and phenyl ring at the 7-position occupy the positions of thymidine bases 805 and 806, thus highlighting the importance of this moiety in blocking the binding of the DNA substrate in the active site. The 3-phenyl ring and the ether-linked phenylpyridine moiety, which extend into the peptide-binding pocket, overlap with residues Y721, N722, Y723, and L724 residues of the TOP1-derived peptide. This highlights the structural importance of this moiety in blocking the binding of the peptide residues. The X-ray structure of the TDP1–**9c** complex provides structural evidence that compound **9c** serves as a tridentate inhibitor of TDP1.

Conclusions

Starting with small molecule microarray-originated imidazopyridine-based TDP1 inhibitors, we utilized a “click”-based oxime diversification protocol to screen a library of aldehyde fragments. This resulted in an initial set of structures that extend the parent imidazopyridine platform to the DNA substrate- and TOP1 peptide-binding channels. The lead oxime (*E*)-**6-D1** shows submicromolar TDP1 inhibition. For a subset of analogs, we replaced oxime linkages with triazole and ether isosteres. Lead compounds, including oxime (*E*)-**6-D1**, triazole **7d** and ether **8b** inhibit TDP1 with selectivity over TDP2 in gel-based *in vitro* assays and they synergize with the TOP1 inhibitor CPT in assays using HCT116 cells. X-ray crystal structures of TDP1 bound to the lead compounds **9a** and **9c** reveal that these small molecules can form hydrogen bonds with the catalytic HKN motifs, while simultaneously extending into both the DNA substrate- and TOP1 peptide-binding grooves. Our findings identify new ways in which small molecules can engage the catalytic pocket, while simultaneously interacting with the DNA

substrate- and TOP1 peptide-binding channels. The trivalent nature of these interactions may provide a basis for developing more efficient multivalent TDP1 inhibitors, which could serve as a new genre of anticancer chemotherapeutics.

Author contributions

XZ and TB conceived the study. XZ designed and synthesized the compounds. WW and EK performed the biological studies. GL performed the X-ray crystallography work. DN performed protein expression work. JT performed protein purification. XZ, WW, GL, EK, YP and TB interpreted the data. XZ, GL, and TB took the lead in writing the manuscript. All authors have provided critical feedback and approved the final manuscript.

Conflicts of interest

Aspects of the work presented are contained within one or more patent applications. The authors declare that there is no conflict of interest.

Acknowledgements

This work was supported in part by Staff Scientist/Staff Clinician Research Award (SSSC-RA) and the NIH Intramural Program, Center for Cancer Research, National Cancer Institute, National Institutes of Health (Z01-BC 006150 and Z01-BC 006198) and the Frederick National Laboratory for Cancer Research, National Institutes of Health under contract 75N91019D00024 (this contract number represents work performed within the scope of the severable FFRDC Bridge contract). We thank James A. Kelley and Christopher C. Lai (Chemical Biology Laboratory, NCI, NIH) for HRMS data collection. We thank the Biophysics Resource in the Center for Structural Biology, NCI at Frederick for use of the LC/ESMS instrument. X-ray diffraction data were collected at the Southeast Regional Collaborative Access Team (SER-CAT) beamline 22-ID at the Advanced Photon Source, Argonne National Laboratory. SER-CAT is supported by its member institutions and equipment grants (S10_RR25528, S10_RR028976 and S10_OD027000) from the National Institutes of Health. Use of the Advanced Photon Source was supported by the US Department of Energy, Office of Science, Office of Basic Energy Sciences under contract no. W-31-109-Eng-38. The content of this publication does not necessarily reflect the views or policies of the Department of Health and Human Services, nor does the mention of trade names, commercial products or organizations imply endorsement by the US Government.

Notes and references

- 1 Y. Pommier, Y. Sun, S.-Y. N. Huang and J. L. Nitiss, *Nat. Rev. Mol. Cell Biol.*, 2016, **17**, 703–721.
- 2 F. Goldwasser, I. Bae, M. Valenti, K. Torres and Y. Pommier, *Cancer Res.*, 1995, **55**, 2116–2121.
- 3 Y. Pommier, *Nat. Rev. Cancer*, 2006, **6**, 789–802.



- 4 S. M. Cuya, M.-A. Bjornsti and R. C. A. M. van Waardenburg, *Cancer Chemother. Pharmacol.*, 2017, **80**, 1–14.
- 5 Y. Pommier and M. Cushman, *Mol. Cancer Ther.*, 2009, **8**, 1008–1014.
- 6 A. Thomas and Y. Pommier, *Clin. Cancer Res.*, 2019, **25**, 6581.
- 7 M. Alagöz, D. C. Gilbert, S. El-Khamisy and A. J. Chalmers, *Curr. Med. Chem.*, 2012, **19**, 3874–3885.
- 8 J. Heo, J. Li, M. Summerlin, A. Hays, S. Katyal, P. J. McKinnon, K. C. Nitiss, J. L. Nitiss and L. A. Hanakahi, *DNA Repair*, 2015, **30**, 28–37.
- 9 H. K. Fam, M. K. Chowdhury, C. Walton, K. Choi, C. F. Boerkoel and G. Henderson, *J. Mol. Histol.*, 2013, **44**, 481–494.
- 10 S.-W. Yang, A. B. Burgin, B. N. Huizenga, C. A. Robertson, K. C. Yao and H. A. Nash, *Proc. Natl. Acad. Sci. U. S. A.*, 1996, **93**, 11534–11539.
- 11 J. Murai, S.-y N. Huang, B. B. Das, T. S. Dexheimer, S. Takeda and Y. Pommier, *J. Biol. Chem.*, 2012, **287**, 12848–12857.
- 12 A. S. Kawale and L. F. Povirk, *Nucleic Acids Res.*, 2018, **46**, 520–537.
- 13 A. Zakharenko, N. Dyrkheeva and O. Lavrik, *Med. Res. Rev.*, 2019, **39**, 1427–1441.
- 14 T. S. Dexheimer, S.-y N. Huang, S. Antony, C. Marchand and Y. Pommier, *Adv. Anticancer Agents Med. Chem.*, 2013, **2**, 444–471.
- 15 S. S. Laev, N. F. Salakhutdinov and O. I. Lavrik, *Bioorg. Med. Chem.*, 2016, **24**, 5017–5027.
- 16 E. J. Brettrager and R. C. A. M. van Waardenburg, *Cancer Drug Resist.*, 2019, **2**, 1153–1163.
- 17 E. Leung, J. Patel, J. A. Hollywood, A. Zafar, P. Tomek, D. Barker, L. I. Pilkington, M. van Rensburg, R. J. Langley, N. A. Helsby, C. J. Squire, B. C. Baguley, W. A. Denny, J. Reynisson and I. K. H. Leung, *Oncol. Ther.*, 2021, **9**, 541–556.
- 18 Y. Zhang, Y. Li, C. Sun, X. Chen, L. Han, T. Wang, J. Liu, X. Chen and D. Zhao, *Cancers*, 2021, **13**, 4002.
- 19 D.-X. Hu, W.-L. Tang, Y. Zhang, H. Yang, W. Wang, K. Agama, Y. Pommier and L.-K. An, *J. Med. Chem.*, 2021, **64**, 7617–7629.
- 20 O. V. Salomatina, I. I. Popadyuk, A. L. Zakharenko, O. D. Zakharova, A. A. Chepanova, N. S. Dyrkheeva, N. I. Komarova, J. Reynisson, R. O. Anarbaev, N. F. Salakhutdinov, O. I. Lavrik and K. P. Volcho, *Steroids*, 2021, **165**, 108771.
- 21 N. S. Dyrkheeva, A. S. Filimonov, O. A. Luzina, A. L. Zakharenko, E. S. Ilina, A. A. Malakhova, S. P. Medvedev, J. Reynisson, K. P. Volcho, S. M. Zakian, N. F. Salakhutdinov and O. I. Lavrik, *Biomolecules*, 2021, **11**, 973.
- 22 J. B. Baell, L. Ferrins, H. Falk and G. Nikolakopoulos, *Aust. J. Chem.*, 2013, **66**, 1483–1494.
- 23 D. A. Erlanson, *J. Med. Chem.*, 2015, **58**, 2088–2090.
- 24 J. B. Baell and J. W. M. Nissink, *ACS Chem. Biol.*, 2018, **13**, 36–44.
- 25 S. L. McGovern, E. Caselli, N. Grigorieff and B. K. Shoichet, *J. Med. Chem.*, 2002, **45**, 1712–1722.
- 26 J. L. Dahlin, J. W. M. Nissink, J. M. Strasser, S. Francis, L. Higgins, H. Zhou, Z. G. Zhang and M. A. Walters, *J. Med. Chem.*, 2015, **58**, 2091–2113.
- 27 R. N. Lindquist, J. L. Lynn and G. E. Lienhard, *J. Am. Chem. Soc.*, 1973, **95**, 8762–8768.
- 28 V. Lopez, T. Stevens and R. N. Lindquist, *Arch. Biochem. Biophys.*, 1976, **175**, 31–38.
- 29 W. Plass, *Angew. Chem., Int. Ed.*, 1999, **38**, 909–912.
- 30 D. R. Davies and W. G. J. Hol, *FEBS Lett.*, 2004, **577**, 315–321.
- 31 D. C. Crans, J. J. Smee, E. Gaidamauskas and L. Yang, *Chem. Rev.*, 2004, **104**, 849–902.
- 32 A. Peck, F. Sunden, L. D. Andrews, V. S. Pande and D. Herschlag, *J. Mol. Biol.*, 2016, **428**, 2758–2768.
- 33 D. R. Davies, H. Interthal, J. J. Champoux and W. G. J. Hol, *Structure*, 2002, **10**, 237–248.
- 34 D. R. Davies, H. Interthal, J. J. Champoux and W. G. J. Hol, *J. Mol. Biol.*, 2002, **324**, 917–932.
- 35 D. R. Davies, H. Interthal, J. J. Champoux and W. G. J. Hol, *Chem. Biol.*, 2003, **10**, 139–147.
- 36 D. R. Davies, H. Interthal, J. J. Champoux and W. G. J. Hol, *J. Med. Chem.*, 2004, **47**, 829–837.
- 37 F. J. Flett, E. Ruksenaite, L. A. Armstrong, S. Bharati, R. Carloni, E. R. Morris, C. L. Mackay, H. Interthal and J. M. Richardson, *Nat. Commun.*, 2018, **9**, 1–13.
- 38 H. Interthal, J. J. Pouliot and J. J. Champoux, *Proc. Natl. Acad. Sci. U. S. A.*, 2001, **98**, 12009–12014.
- 39 N. Dyrkheeva, R. Anarbaev, N. Lebedeva, M. Kuprushkin, A. Kuznetsova, N. Kuznetsov, N. Rechkunova and O. Lavrik, *Front. Cell. Develop. Biol.*, 2020, **8**, 1427.
- 40 E. Q. Comeaux and R. C. A. M. van Waardenburg, *Drug Metab. Rev.*, 2014, **46**, 494–507.
- 41 A. C. Raymond, M. C. Rideout, B. Staker, K. Hjerrild and A. B. Burgin, *J. Mol. Biol.*, 2004, **338**, 895–906.
- 42 V. M. Krishnamurthy, L. A. Estrofi and G. M. Whitesides, in *Fragment-based Approaches in Drug Discovery*, ed. W. J. A. D. A. Erlanson, Wiley-VCH GmbH & Co., Weinheim, DE, 2006, pp. 11–53.
- 43 C. Chittasupho, *Therap. Deliv.*, 2012, **3**, 1171–1187.
- 44 C. A. Lipinski, F. Lombardo, B. W. Dominy and P. J. Feeney, *Adv. Drug Delivery Rev.*, 2001, **46**, 3–26.
- 45 I. V. Hartung, B. R. Huck and A. Crespo, *Nat. Rev. Chem.*, 2023, **7**, 3–4.
- 46 T. S. Elliott, A. Slowey, Y. Ye and S. J. Conway, *MedChemComm*, 2012, **3**, 735–751.
- 47 G. T. Lountos, X. Z. Zhao, T. R. Burke, E. Kiselev, Y. Pommier, J. E. Tropea, D. Needle and D. S. Waugh, *Nucleic Acids Res.*, 2019, **47**, 10134–10150.
- 48 X. Z. Zhao, E. Kiselev, G. T. Lountos, W. Wang, J. E. Tropea, D. Needle, T. A. Hilimire, J. S. Schneekloth, D. S. Waugh, Y. Pommier and T. R. Burke, *Chem. Sci.*, 2021, **12**, 3876–3884.
- 49 H. C. Kolb, M. G. Finn and K. B. Sharpless, *Angew. Chem., Int. Ed.*, 2001, **40**, 2004–2021.
- 50 M. King and A. Wagner, *Bioconjugate Chem.*, 2014, **25**, 825–839.
- 51 A. Bruylants and E. Feytmants-de Medicis, *Carbon-Nitrogen Double Bonds*, 1970, 465–504, DOI: [10.1002/9780470771204.ch10](https://doi.org/10.1002/9780470771204.ch10).
- 52 J. Kalia and R. T. Raines, *Angew. Chem., Int. Ed.*, 2008, **47**, 7523–7526.



- 53 S. Ulrich, D. Boturyn, A. Marra, O. Renaudet and P. Dumy, *Chem. – Eur. J.*, 2014, **20**, 34–41.
- 54 D. K. Kölmel and E. T. Kool, *Chem. Rev.*, 2017, **117**, 10358–10376.
- 55 M. Bahta, F. Liu, S.-E. Kim, A. G. Stephen, R. J. Fisher and T. R. Burke, Jr., *Nat. Protoc.*, 2012, **7**, 686–702.
- 56 X. Z. Zhao, D. Hymel and T. R. Burke, Jr., *Bioorg. Med. Chem. Lett.*, 2016, **26**, 5009–5012.
- 57 X. Z. Zhao, D. Hymel and T. R. Burke, Jr., *Bioorg. Med. Chem.*, 2017, **25**, 5041–5049.
- 58 X. Z. Zhao, T. R. Burke, Jr. and F. Liu, *Molecules*, 2020, **25**, 2807.
- 59 P. T. Corbett, J. Leclaire, L. Vial, K. R. West, J.-L. Wietor, J. K. M. Sanders and S. Otto, *Chem. Rev.*, 2006, **106**, 3652–3711.
- 60 H. Bienaymé and K. Bouzid, *Angew. Chem., Int. Ed.*, 1998, **37**, 2234–2237.
- 61 C. Blackburn, B. Guan, P. Fleming, K. Shiosaki and S. Tsai, *Tetrahedron Lett.*, 1998, **39**, 3635–3638.
- 62 K. Groebke, L. Weber and F. Mehlh, *Synlett*, 1998, 661–663.
- 63 S. Shaaban and B. F. Abdel-Wahab, *Mol. Diversity*, 2016, **20**, 233–254.
- 64 C. G. McCarty, *Carbon–Nitrogen Double Bonds*, 1970, pp. 363–464, DOI: [10.1002/9780470771204.ch9](https://doi.org/10.1002/9780470771204.ch9).
- 65 H. Sharghi and M. H. Sarvari, *Synlett*, 2001, 0099–0101.
- 66 J. Dhuguru, E. Zviagin and R. Skouta, *Pharmaceuticals*, 2022, **15**, 66.
- 67 N. A. Meanwell, in *Tactics in Contemporary Drug Design*, ed. N. A. Meanwell, Springer Berlin Heidelberg, Berlin, Heidelberg, 2015, pp. 283–381, DOI: [10.1007/9783642313292_29](https://doi.org/10.1007/9783642313292_29).
- 68 M. S. Malik, S. A. Ahmed, I. I. Althagafi, M. A. Ansari and A. Kamal, *RSC Med. Chem.*, 2020, **11**, 327–348.
- 69 R. P. Wurz, K. Dellamaggiore, H. Dou, N. Javier, M.-C. Lo, J. D. McCarter, D. Mohl, C. Sastri, J. R. Lipford and V. J. Cee, *J. Med. Chem.*, 2018, **61**, 453–461.
- 70 G. B. McGaughey, M. Gagné and A. K. Rappé, *J. Biol. Chem.*, 1998, **273**, 15458–15463.
- 71 S. E. Wheeler and K. N. Houk, *Mol. Phys.*, 2009, **107**, 749–760.
- 72 T. Chen, M. Li and J. Liu, *Cryst. Growth Des.*, 2018, **18**, 2765–2783.
- 73 U. Samanta, D. Pal and P. Chakrabarti, *Acta Crystallogr., Sect. D: Biol. Crystallogr.*, 1999, **D55**, 1421–1427.
- 74 A. Sengupta, R. Mahalakshmi, N. Shamala and P. Balaram, *J. Pept. Res.*, 2005, **65**, 113–129.
- 75 M. Brylinski, *Chem. Biol. Drug Des.*, 2018, **91**, 380–390.
- 76 C. R. Forbes, S. K. Sinha, H. K. Ganguly, S. Bai, G. P. A. Yap, S. Patel and N. J. Zondlo, *J. Am. Chem. Soc.*, 2017, **139**, 1842–1855.
- 77 M. W. Krone, C. R. Travis, G. Y. Lee, H. J. Eckvahl, K. N. Houk and M. L. Waters, *J. Am. Chem. Soc.*, 2020, **142**, 17048–17056.

